EDGE ARTICLE

Check for updates

Core-dependent properties of copper nanoclusters: valence-pure nanoclusters as NIR TADF emitters and mixed-valence ones as semiconductors†

Leon Li-Min Zhang,‡[a] Guodong Zhou, [ID] ‡[b] Guoqing Zhou,[c] Hung-Kay Lee,[a] Ni Zhao, [ID] [b] Oleg V. Prezhdo [ID] [c] and Thomas C. W. Mak [ID] *[a]

We report herein that copper alkynyl nanoclusters show metal-core dependent properties *via* a charge-transfer mechanism, which enables new understanding of their structure–property relationship. Initially, nanoclusters **1** and **2** bearing respective $Cu(I)_{15}$ (**C1**) and $Cu(I)_{28}$ (**C2**) cores were prepared and revealed to display near-infrared (NIR) photoluminescence mainly from the mixed alkynyl → Cu(I) ligand-to-metal charge transfer (LMCT) and cluster-centered transition, and they further exhibit thermally activated delayed fluorescence (TADF). Subsequently, a vanadate-induced oxidative approach to *in situ* generate a nucleating Cu(II) cation led to assembly of **3** and **4** featuring respective $[Cu(II)O_6]@Cu(I)_{47}$ (**C3**) and $\{[Cu(II)O_4]\cdot[VO_4]_2\}@Cu(I)_{46}$ (**C4**) cores. While interstitial occupancy of Cu(II) triggers inter-valence charge-transfer (IVCT) from Cu(I) to Cu(II) to quench the photoluminescence of **3** and **4**, such a process facilitates charge mobility to render them semiconductive. Overall, metal-core modification results in an interplay between charge-transfer processes to switch TADF to semiconductivity, which underpins an unusual structure–property correlation for designed synthesis of metal nanoclusters with unique properties and functions.

Introduction

Amid rapid expansion of research endeavor into nanoscale materials, atomically precise metal nanoclusters have attracted considerable interest.[1] They not only motivate continuous efforts in the chemical community to achieve ever-evolving compositional and structural complexity, but also serve as an inspiration to materials scientists due to their use in a variety of emerging technological applications.[2] In particular, their precise structural nature facilitates deeper understanding of the structure–property relationship, which has direct ramifications for design of functional nanomaterials.[3,4]

In this regard, the copper alkynyl nanoclusters constitute a good research platform owing to their versatile self-assembled

[a]Department of Chemistry and Center of Novel Functional Molecules, The Chinese University of Hong Kong, Hong Kong SAR, People's Republic of China. E-mail: tcwmak@cuhk.edu.hk

[b]Department of Electronic Engineering, The Chinese University of Hong Kong, Hong Kong SAR, People's Republic of China

[c]Department of Chemistry, University of Southern California, Los Angeles, California 90089-1062, USA

nanostructures and appealing physio-chemical properties in photoluminescence, catalysis, biomedical sensing and electronics.[5] However, such a goal is currently far from reach. For example, while it is presumed that copper alkynyl nanoclusters would exhibit exotic photoluminescence performances, relevant investigations are very preliminary, and key studies are still mechanistic in nature.[5] Nevertheless, some impressive progress has been made in the recent literature. Scott and Hayton reported $[Cu_{20}(PhC\equiv C)_{12}(OAc)_6]$ as an effective catalyst for [3 + 2] cycloadditions between alkynes and azides.[6] Zheng reported that $[Cu_{53}(CF_3COO)_{10}(^tBuC\equiv C)_{20}Cl_2H_{18}]^+$ was used as an effective precursor to generate γ-CuI films as perovskite solar cells.[7] These results imply the potentiality of diversified yet underexplored attributes of copper alkynyl nanoclusters.

We have previously established a comproportionation reaction methodology and focused on the structural role of anionic species to enhance the size and nuclearity of copper(I) alkynyl nanoclusters.[8] In this work, we make inroads to comparative synthesis of valence-pure and mixed-valence copper nanoclusters that exhibit metal-core dependent material properties *via* a charge-transfer mechanism, which enables new understanding of their structure–property relationship.

Initially, the comproportionation reaction furnished nanoclusters $[Cu(I)_{15}(^tBuC\equiv C)_{14}NO_3]$ (**1**) and $[Cu(I)_{28}(^tBuC\equiv C)_{22}(SO_4)_2(OMe)_2]$ (**2**). They were revealed to exhibit NIR

photoluminescence mainly from the mixed alkynyl → Cu(I) LMCT and cluster-centered transition and further exhibit TADF. To the best of our knowledge, **1** and **2** constitute the first examples of coinage-metal nanoclusters displaying NIR TADF. Subsequently, a vanadate-assisted approach to *in situ* generate a nucleating Cu(II) cation was developed in conjugation with the comproportionation reaction to assemble $\{[Cu(II)O_6]@Cu(I)_{47}(^iPrC≡C)_{33}\}(ClO_4)_4$ (**3**) and $\{[Cu(II)O_4][VO_4]_2@Cu(I)_{46}(^tBuC≡C)_{27}(^tBuPO_3)_2(H_2O)\}(BF_4)_3(CH_2Cl_2)_2(Et_2O)_2(H_2O)$ (**4**). While interstitial incorporation of Cu(II) triggers IVCT from Cu(I) to Cu(II) to quench the photoluminescence of **3** and **4**, such a process facilitates charge mobility to render them semi-conductive. Overall, metal-core modification originating from the interplay of the charge-transfer process causes a switch from TADF to semiconductivity. Such pros and cons effect of Cu(II) cations on cluster properties not only advances our knowledge on the structure–property relationship of atomically precise metal nanoclutructursters, but also provides a potential route to tailor future development of function-specific nanoclusters.

Results and discussion

Synthesis and characterization

While the structures of nanoclusters dictate their physio-chemical behavior,[9] a systematic synthetic study based on a proven methodology is not just a routine exercise, but it aims to obtain novel nanoclusters with desirable properties. Herein, screening the Cu(II) source of the comproportionation reaction $Cu(0)/Cu(II)/^tBuC≡CH$ furnished two valence-pure Cu(I) nanoclusters (Scheme 1, upper part). Use of Cu(II) $(NO_3)_2$ at room temperature yielded red crystals of $[Cu(I)_{15}(^tBuC≡C)_{14}NO_3]$ (**1**).

During revision of this manuscript, synthesis of **1** was reported by Xie and Lu.[10] Single-crystal X-ray diffraction analysis (SCXD) revealed that the Cu(I)$_{15}$ (**C1**) core of **1** is stabilized by 14 alkynyl ligands and one μ-κO:κO′ NO_3^- with Cu(I)–O bond lengths of 2.169 and 2.379 Å (Fig. 1a). By using Cu(II)SO_4 in the solvothermal reaction, $[Cu(I)_{28}(^tBuC≡C)_{22}(SO_4)_2(OMe)_2]$ (**2**) was obtained as yellow crystals. Notably, **2** cannot be obtained without solvothermal treatment, presumably because its formation involving deprotonation of MeOH to the MeO^- bridging ligand does not readily occur under ambient conditions. As shown in Fig. 1b, in addition to 22 alkynyl ligands, two μ$_3$-MeO$^-$ and two μ$_3$-κO:κO′:κO″ SO_4^{2-} ligands cap the respective central and terminal section of the Cu(I)$_{28}$ (**C2**) core to assemble **2** as an elongated nanorod. In addition to its significant structural diversity, **2** also represents the highest-nuclearity Cu(I) alkynyl cluster assembled without an interstitial species.[5d] The Cu(I)–O bond distances span the range 1.925–2.140 Å.

Based on the comproportionation reaction to form Cu(I) nanoclusters, we have previously introduced polyoxomolybdate (POMo) to synthesize POMo@Cu(I) nanoclusters.[8a] Herein, an attempt to introduce polyoxovanadate (POV)[11] by using Na$_3$-VO$_4$/$^tBuPO_3H_2$ yielded unprecedented Cu(II)-containing Cu(I) nanoclusters **3** and **4** (Scheme 1, upper part). Control experiments were conducted to probe the formation path for the Cu(II) cation. As illustrated in the lower part of Scheme 1, in step (i) Na$_3$VO$_4$/$^tBuPO_3H_2$ reacted to form a decavanadate hydronium compound $[V_{10}O_{28}]_2·[H_3O]_{12}$, which has not been reported prior to this work; in step (ii) $[V_{10}O_{28}]_2·[H_3O]_{12}$ oxidized Cu(0) to *in situ* generate Cu(II) (see details in the ESI†). The Cu(II) generated *via* such a POV-assisted route consequently serves as a nucleating cation to form the mixed-valence nanoclusters **3** and **4**.

In the synthesis of **3**, a one-pot reaction of Na$_3$VO$_4$/$^tBuPO_3H_2$ and Cu(0)/Cu(II)(ClO$_4$)$_2$/$^iPrC≡CH$ in methanol yielded a yellow precipitate that was re-dissolved in dichloromethane, to which
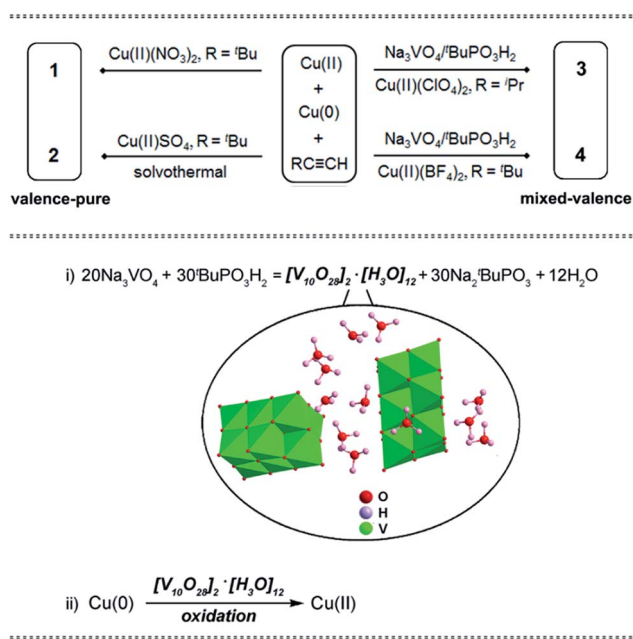
Scheme 1 Upper: synthetic routes of copper nanoclusters **1–4**. Lower: the vanadate-induced formation pathway of the nucleating Cu(II) cation in **3** and **4**.
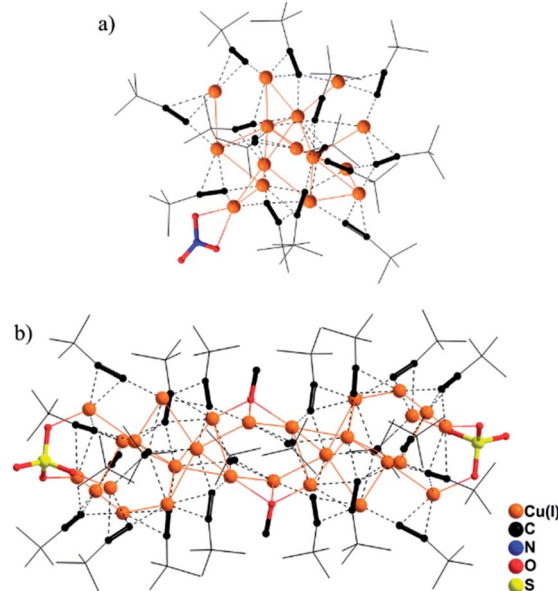

Fig. 1 Molecular structures of (a) **1**; (b) **2**.

slow diffusion of diethyl ether afforded deep red crystals of $\{[Cu(II)O_6]@Cu(I)_{47}(^iPrC{\equiv}C)_{33}\}\cdot(ClO_4)_4$ (**3**). As shown in Fig. 2a, the central Cu(II) cation, Cu1, is stabilized within the Cu(I) shell by forming Cu(I)–O–Cu(II) bonding interactions (Fig. S12†). The octahedral coordination environment of Cu1 exhibits significant Jahn–Teller distortion (Fig. S12†), where atoms O1–O4 are equatorial donors with Cu(II)–O bond lengths of 1.940–1.957 Å, and O5 and O6 are axial donors with elongated distances of 2.325 and 2.635 Å, respectively. Bond-valence sum (BVS) calculation gives a calculated value of 2.18 for Cu1 (Table S2†).[12] The +II oxidation state of Cu1 is further confirmed by the EPR spectrum (Fig. 2b), where it shows four-line splitting with $g_{\parallel}$

$(2.310) > g_{\perp}$ $(2.053) > g_e$ (2.0023), and $A_{\parallel} = 135$ G typical of Cu(II) axial signals in the $d_{x^2-y^2}$ ground state,[13] which is in accordance with the elongated octahedral coordination geometry of Cu1. This $\{[Cu(II)O_6]@Cu(I)_{47}\}$ (**C3**) core is shielded by 33 peripheral $^iPrC{\equiv}C^-$ ligands (Fig. 2a).

In light of the alkynyl ligand effect on cluster assembly, $^iPrC{\equiv}CH$ was replaced by $^tBuC{\equiv}CH$ in the synthesis. Accordingly, the reaction of $Na_3VO_4/^tBuPO_3H_2$ with $Cu(0)/Cu(II)(BF_4)_2/^tBuC{\equiv}CH$ yielded a disparate nanocluster $\{[Cu(II)O_4]\cdot[VO_4]_2@Cu(I)_{46}(^tBuC{\equiv}C)_{27}(^tBuPO_3)_2(H_2O)\}\cdot(BF_4)_3\cdot(CH_2Cl_2)_2\cdot(Et_2O)_2\cdot(H_2O)$ (**4**). As seen in Fig. 2c, Cu1 is also encased inside the cavity of the nanocluster that is sandwiched by two $[VO_4]^{3-}$ anions. It exhibits a distorted square-planar coordination geometry with Cu(II)–O bond lengths of 1.913(6)–1.945(6) Å (Fig. S12†), and BVS analysis supports its +II oxidation state (calc. 2.04, Table S2†). In the EPR spectrum of **4** (Fig. 2b), the axial signals $g_{\parallel}$ $(2.280) > g_{\perp}$ $(2.040) > g_e$ (2.0023) and $A_{\parallel} = 150$ G are in agreement with the observed coordination environment of Cu1. Extensive Cu(I)–O–Cu(II) connectivity (Fig. S12†) consolidates the $\{[Cu(II)O_4]\cdot[VO_4]_2\}$ $@Cu(I)_{46}$ (**C4**) core, which is further protected by 27 $^tBuC{\equiv}C^-$ and 2 μ_4-$\kappa O{:}\kappa O'{:}\kappa O'{:}\kappa O''$ $^tBuPO_3{}^{2-}$ peripheral struts.

Photophysical and optical properties

The valence-pure **1** and **2**, and mixed-valence **3** and **4** offer a new basis to explore the structure–property relationship. In this
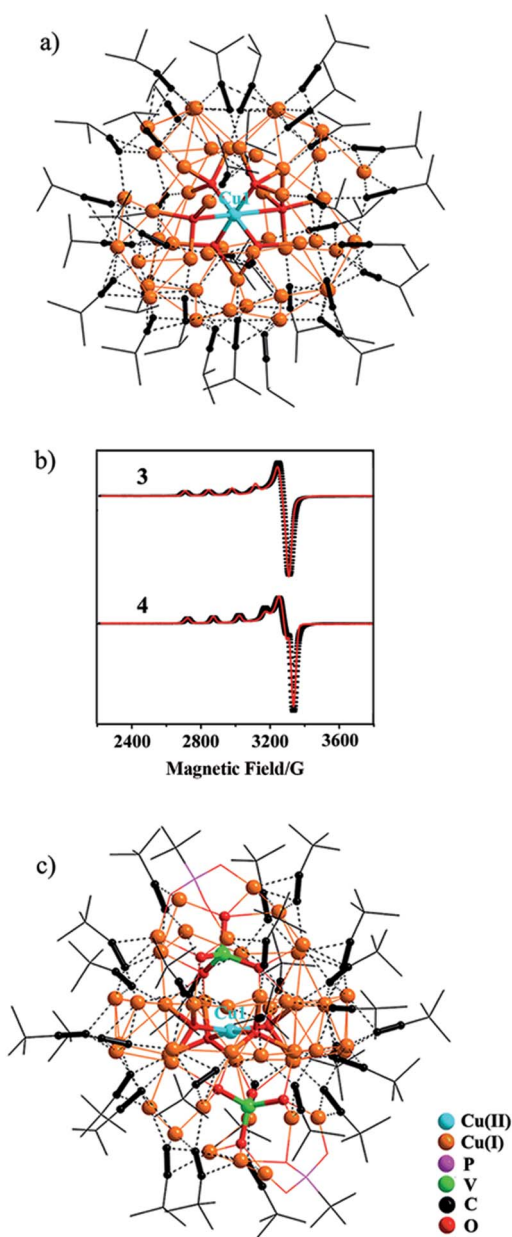
Fig. 2 Molecular structures of (a) **3**; (c) **4**. The Cu(II)−O−Cu(I) bonding interactions in **3** and **4** are highlighted as thicker bonds. (b) EPR spectra of **3** and **4**. Black and red lines represent the experimental and simulated EPR patterns, respectively.

Fig. 3 3D Excitation-emission correlation spectra of (a) **1** and (d) **2** monitored in the solid state at 298 K. Temperature-dependent emission profiles of (b) **1** and (e) **2**. Temperature-dependent emission decay time of (c) **1** and (f) **2**; the solid line represents Boltzmann fitting to the experimental data.

vein, photoluminescence as one of the most important properties was first studied. As a result, while valence-pure nanoclusters show NIR TADF, mixed-valence ones do not emit, indicating that incorporation of Cu(II)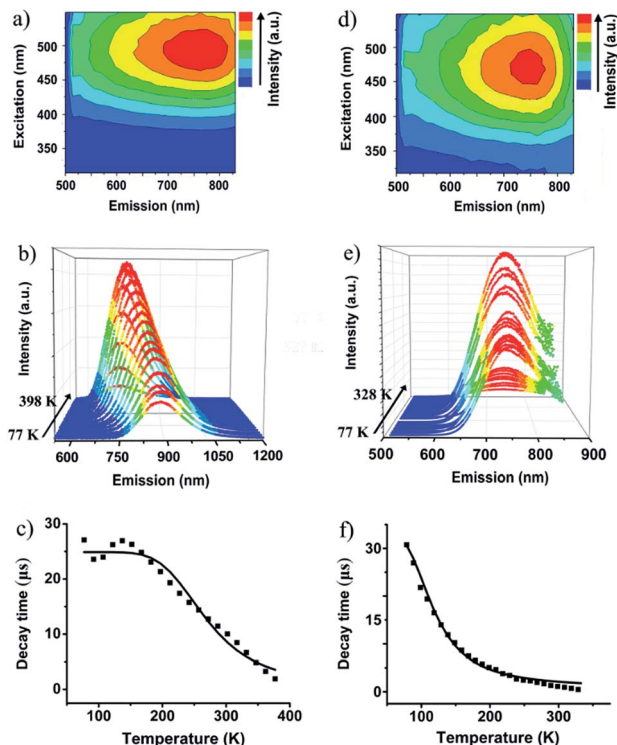 has quenched the photoluminescence. Fig. 3a and d show the 3D excitation–emission correlation spectra recorded for crystalline samples of **1** and **2** at 298 K, which exhibit excitation windows with maximum wavelengths at 500 and 475 nm, respectively. In their temperature-dependent emission profiles, while **1** largely blue-shifted upon increasing temperature, **2** only exhibited a marginal blue-shift. As shown in Fig. 3b, upon excitation at 500 nm at 77 K, **1** featured a board NIR emission band centered at 871 nm. With increasing temperature, a continuous bathochromic effect occurred to afford at 398 K an emission maximum at 731 nm. The luminescence intensity grew persistently from 77 K to peak at 298 K and then started to decline, where the identifiable emission maximum at 731 nm was observed at 398 K. When heated from 77 to 328 K, the emission maximum of **2** blue-shifted from 748 to 738 nm (Fig. 3e). In this process, the luminescence intensity increased from 77 K to culminate at 208 K and then decreased. Above 328 K, luminescence became too weak to be identified.

The blue-shifting trend with increasing temperature is suggestive of a TADF mechanism for Cu(I) clusters **1** and **2**.[14] In this context, the temperature-dependent emission decay time was measured (Fig. 3c and f), and their correlation was studied with the Boltzmann equation derived from the TADF model:

$$\tau = \frac{[3 + \exp(\Delta E(S_1 - T_1)/k_B T)]}{\left[3/\tau(T_1) + 1\big/\tau(S_1)^* \exp(\Delta E(S_1 - T_1)/k_B T)\right]}$$

where τ, $\tau(S_1)$, $\tau(T_1)$, k_B, $\Delta E(S_1 - T_1)$ and T represent the observed lifetime, singlet state decay lifetime, triplet state decay lifetime, Boltzmann constant, singlet-triplet energy separation and temperature, respectively. The crucial parameter of singlet-triplet energy separation $\Delta E(S_1 - T_1)$ is generally required to be <3000 cm^{-1}/0.37 eV for occurrence of TADF.[14,15] As a result, data fitting gave $\Delta E(S_1 - T_1) = 1200$ cm^{-1}/0.15 eV, $\tau(T_1) = 25$ μs and $\tau(S_1) = 14$ ns for **1**. For **2**, values of $\Delta E(S_1 - T_1) = 380$ cm^{-1}/0.047 eV, $\tau(T_1) = 33.5$ μs and $\tau(S_1) = 115$ ns were extracted. These values demonstrate that TADF occurred with reverse inter-system crossing (RISC) from the triplet state T_1 to the singlet manifold S_1. Furthermore, variation of emission intensity as a function of temperature also substantiates an equilibrium between the T_1 state and S_1 state.[16] As mentioned above, the emission intensity shows a bell shape from low to high temperature (Fig. 3b and e). This is due to up-conversion of the T_1 to S_1 state upon increasing the temperature (increasing intensity), followed by thermal vibration to depopulate the excited state at higher temperature (decreasing intensity). It is worth noting that **1** and **2** represent the first examples of high-nuclearity metal clusters displaying NIR TADF, and this implies that the photoluminescence attributes of Cu(I) alkynyl nanoclusters are favorable.

DFT calculations were performed with the Vienna *Ab initio* Simulation Package (VASP)[17] to gain insight into the photophysical properties of **1** and **2**, where their whole molecular structures remained intact. The Perdew–Burke–Ernzerhof (PBE) exchange-correlation functional and projector augmented wave (PAW) method were employed with an energy cutoff of 500.0 eV.[18] For computational efficiency, a single nanocluster of **1** and **2** was extracted and padded with 10 Å in x, y, and z directions, and the gamma point was used to sample the Brillouin zone. The optimized geometries of the ground state of **1** and **2** are comparable to those determined by X-ray crystallographic analysis. For example, the computed structure of **1** gave bond lengths of Cu12–O1 2.348 and Cu12–O2 2.118 Å, which are close to the respective values of 2.379 and 2.169 Å in the crystal structure. The highest occupied molecular orbital (HOMO) and lowest unoccupied molecular orbital (LUMO) of **1** and **2** are shown in Fig. 4. For **1**, the HOMO is predominantly distributed over the nitrate oxygen atoms and their coordinated Cu(I) atoms, whereas the LUMO resides on the remaining Cu(I) atoms with some population on the ^{t}BuC≡C$^-$ ligands. For **2**, the HOMO is dominated by the sulfate oxygen atoms and their coordinated Cu(I) atoms and ^{t}BuC≡C$^-$ ligands, and the LUMO is contributed by Cu(I) atoms and ^{t}BuC≡C$^-$ ligands. Thus the emissions of **1** and **2** originating from LUMO to HOMO charge transfer mainly involve a mixed ^{t}BuC≡C$^-$ → Cu(I) LMCT and cluster-centered transition. This result is in agreement with that of [Cu(I)]$_{15}$(^{t}BuC≡C)$_{10}$(CF$_3$COO)$_5$]·^{t}BuC≡CH reported by Sun.[19]

To contextualize the quenching effect of Cu(II) on photoluminescence properties, we compared the optical properties of **1–2** with **3–4**. Fig. 5 shows the UV-Vis-NIR spectra measured in the solid state. While **1** and **2** show no indication of NIR absorption, **3** and **4** exhibit prominent bands in the NIR region 700–1200 nm, which evidently stem from incorporation of Cu(II). According to the DFT calculation and reported metal alkynyl clusters, the visible-light absorption in 300–600 nm for **1–4** is attributed to various charge transfer transitions including π → π* acetylide, cluster-centered, MLCT and LMCT interactions.[19a,20] In contrast, the NIR absorption of **3** and **4** is assigned to IVCT from Cu(I) (3d^{10}) to Cu(II) (3d^9). Such IVCT was achieved by the Cu(I)–O–Cu(II) linkage as described above.[20] The fact that **3** and **4** do not emit also provides spectral evidence for
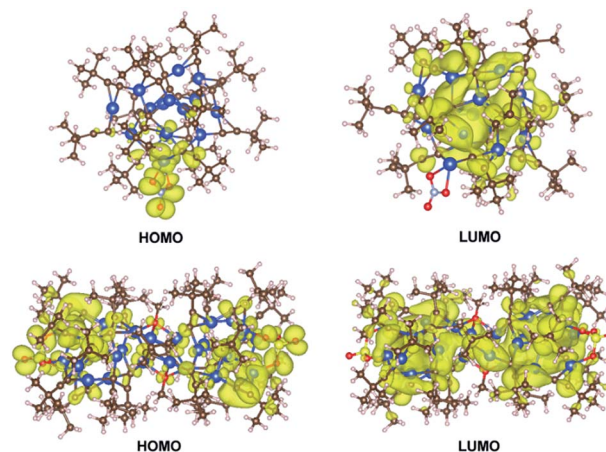

Fig. 4 Frontier molecular orbitals of **1** (upper) and **2** (lower) at the ground state.

a charge-transfer quenching mechanism, that is, the characteristic photoluminescence of **3** and **4** originating from the alkynyl → Cu(I) LMCT and cluster-centered transition was switched off by the subsequent Cu(I) → Cu(II) IVCT transition.[21]

Dielectric and electrical properties

The divergent photophysical properties of **1–2** from **3–4** demonstrate that their metal cores tailor the materials' bulk behavior. This prompts us to further explore their dielectric and electrical properties, which have been less studied in metal nanoclusters owing to their instability in the fabrication of high-quality thin films.[22] In this vein, bulk crystalline samples of **1–4** were each prepared as a pellet and sandwiched between Cu and Al electrodes to fabricate an electronic device for measurements (Fig. 6a). As shown in Fig. 6b, **1** and **2** display frequency-independent dielectric behavior with a dielectric constant of about 5.0, which corresponds to a low-dielectric state. By contrast, drastic response to frequency was detected from 10^3 and 10^2 Hz for **3** and **4**, which gave at 20 Hz high dielectric constants of 3800 and 1500, respectively. For reference, $[Cu(I)_{17}(^tBuC{\equiv}C)_{16}MeOH]{\cdot}BF_4$ with a cation–anion structure showed similar dielectric behavior to neutral nanoclusters **1** and **2** (Fig. S11†). This excludes the possibility that the high-dielectric state of **3** and **4** originates from cation/anion movement under an applied electric field. Instead, it is attributed to interfacial polarization dictated by the presence/distribution of Cu(II) cations and O^{2-} anions with large dipole moments.

The temperature-dependent electrical conductivities of **1–4** were measured using a two-probe current–voltage (*I–V*) technique. At ambient temperature, **1** and **2** show low conductivities of 3.19×10^{-11} and 6.09×10^{-11} S m^{-1}, which upon increasing the temperature to 100 °C increased to 2.57×10^{-8} and 2.29×10^{-9} S m^{-1}, respectively. The *I–V* curves show a linear characteristic in the measured temperature range (Fig. 6c). As seen in Fig. 6d, the corresponding Arrhenius fit to data in the linear regime provides activation energies of 1.06 eV for **1** and 0.97 eV for **2**, suggesting that both are electrical insulators. In contrast, the ambient temperature conductivities of **3** and **4** are significantly higher at 1.01×10^{-6} and 1.24×10^{-8} S m^{-1} and enhanced over a temperature range of 80 °C to attain $2.33 \times$
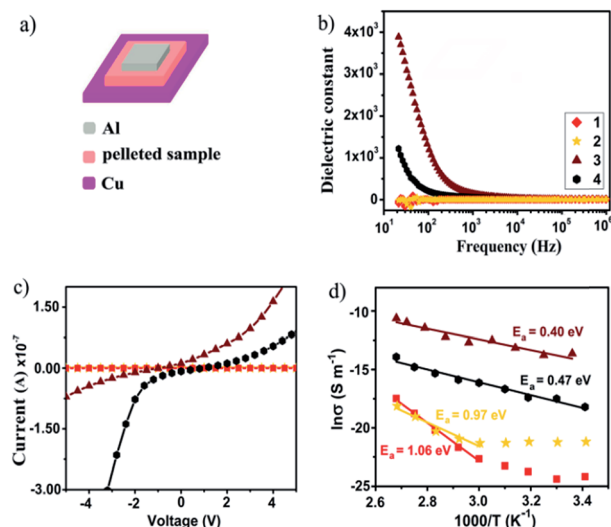

Fig. 6 (a) Fabrication of an electronic device for dielectric and electrical measurements. (b) Frequency-dependent dielectric constants of **1–4** recorded at room temperature. (c) Current–voltage curves recorded at room temperature. (d) Temperature-dependent electrical conductivity; straight lines represent Arrhenius fitting to the experimental data.

10^{-5} and 9.04×10^{-7} S m^{-1}, respectively. As such, **3** and **4** show two to four orders of magnitude increased ambient-temperature conductivities over **1** and **2**. The logarithm of conductivity and inverse temperature displays a linear relationship, which indicates that **3** and **4** are thermally activated semiconductors. The activation energy was fitted to be 0.40 eV for **3** and 0.47 eV for **4**. The electrical conductivities of **3** and **4** are comparable to those of semiconductive Cu(II) materials with moderate conductivity.[23] Their enhanced electrical conductivities are likely due to interstitial incorporation of a Cu(II) cation as the electron acceptor to trigger IVCT that follows LMCT to facilitate charge mobility,[24] where the Cu(II) cation should be chemically stabilized by ligand oxygen atoms within the Cu(I) shell. These results suggest that the electrical nature of Cu(I) nanoclusters can be modified by incorporating a trace amount of Cu(II) as the dopant, which may facilitate the search for suitable metal nanoclusters as new semiconducting materials.

Conclusions

In summary, we have prepared mixed-valence Cu(II)/Cu(I) nanoclusters *via* a vanadate-assisted oxidative procedure for comparison with related valence-pure Cu(I) nanoclusters. The charge-transfer processes occurring within these two types of nanoclusters dominate their photophysical, dielectric and electrical properties. Particularly, while the valence-pure nanoclusters exhibit near-infrared thermally activated delayed fluorescence, the mixed-valence ones display semiconductivity. These results not only demonstrate the feasibility to modify the metal core to engender distinct desirable properties, but also facilitate rationalization of the structure–property relationship for future development of function-specific metal nanoclusters.
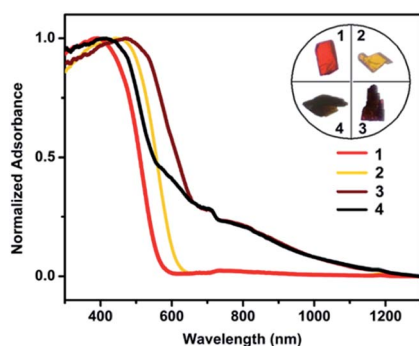

Fig. 5 UV-Vis-NIR diffuse reflectance spectra of **1–4** measured in the solid state. Inset: appearance of single crystals under ambient light.

Conflicts of interest

There are no conflicts to declare.

Acknowledgements

Notes and references

1 (a) Z. Lei, X.-K. Wan, S.-F. Yuan, Z.-J. Guan and Q.-M. Wang, *Acc. Chem. Res.*, 2018, **51**, 2465; (b) R. S. Dhayal, W. E. van Zyl and C. W. Liu, *Acc. Chem. Res.*, 2016, **49**, 86; (c) Z. B. Gan, N. Xia and Z. K. Wu, *Acc. Chem. Res.*, 2018, **51**, 2774; (d) Q.-M. Wang, Y.-M. Lin and K.-G. Liu, *Acc. Chem. Res.*, 2015, **48**, 1570; (e) Q. Li, M. Zhou, W. Y. So, J. C. Huang, M. X. Li, D. R. Kauffman, M. Cotlet, T. Higaki, L. A. Peteanu, Z. Z. Shao and R. Jin, *J. Am. Chem. Soc.*, 2019, **141**, 5314; (f) X. Kang, S. X. Wang, Y. B. Song, S. Jin, G. D. Sun, H. Z. Yu and M. Z. Zhu, *Angew. Chem., Int. Ed.*, 2016, **55**, 3611; (g) T. A. Nguyen, Z. R. Jones, B. R. Goldsmith, W. R. Buratto, G. Wu, S. L. Scott and T. W. Hayton, *J. Am. Chem. Soc.*, 2015, **137**, 13319.

2 (a) X. Liu and D. Astruc, *Coord. Chem. Rev.*, 2018, **359**, 112; (b) X. Kang and M. Zhu, *Chem. Soc. Rev.*, 2019, **48**, 2422; (c) V. W.-W. Yam and K. K.-W. Lo, *Chem. Soc. Rev.*, 1999, **28**, 323; (d) X. Yuan, Z. Luo, Y. Yu, Q. Yao and J. Xie, *Chem.–Asian J.*, 2013, **8**, 858; (e) Z.-H. Chen, L.-Y. Zhang and Z.-N. Chen, *Organometallics*, 2012, **31**, 256; (f) J.-W. Liu, L. Feng, H.-F. Su, Z. Wang, Q.-Q. Zhao, X.-P. Wang, C.-H. Tung, D. Sun and L.-S. Zheng, *J. Am. Chem. Soc.*, 2018, **140**, 1600; (g) Z. Wang, H.-F. Su, C.-H. Tung, D. Sun and L.-S. Zheng, *Nat. Commun.*, 2018, **9**, 4407; (h) S.-S. Zhang, H.-F. Su, G.-L. Zhuang, X.-P. Wang, C.-H. Tung, D. Sun and L.-S. Zheng, *Chem. Commun.*, 2018, **54**, 11905; (i) Z. Wang, H.-F. Su, Y.-Z. Tan, S. Schein, S.-C. Lin, W. Liu, S.-A. Wang, W.-G. Wang, C.-H. Tung, D. Sun and L.-S. Zheng, *Proc. Natl. Acad. Sci. U. S. A.*, 2017, **114**, 12132.

3 (a) R. Jin, *Nanoscale*, 2015, **7**, 1549; (b) M. Zhu, C. M. Aikens, F. J. Hollander, G. C. Schatz and R. Jin, *J. Am. Chem. Soc.*, 2008, **130**, 5883; (c) W.-H. Fang, L. Zhang and J. Zhang, *J. Am. Chem. Soc.*, 2016, **138**, 7480; (d) H. N. Miras, J. Yan, D.-L. Long and L. Cronin, *Chem. Soc. Rev.*, 2012, **41**, 7403; (e) D.-L. Long, E. Burkholdera and L. Cronin, *Chem. Soc. Rev.*, 2007, **36**, 105; (f) K.-G. Liu, S.-K. Chen, Y.-M. Lin and Q.-M. Wang, *Chem. Commun.*, 2015, **51**, 9896.

4 (a) S. Hossain, Y. Niihori, L. V. Nair, B. Kumar, W. Kurashige and Y. Negishi, *Acc. Chem. Res.*, 2018, **51**, 3114; (b) Y. Negishi, W. Kurashige, Y. Niihori and K. Nobusada, *Phys. Chem. Chem. Phys.*, 2013, **15**, 18736; (c) S. Wang, Y. Song, S. Jin, X. Liu, J. Zhang, Y. Pei, X. Meng, M. Chen, P. Li and M. Zhu, *J. Am. Chem. Soc.*, 2015, **137**, 4018; (d) G. Soldan, M. A. Aljuhani, M. S. Bootharaju, L. G. AbdulHalim, M. R. Parida, A.-H. Emwas, O. F. Mohammed and O. M. Bakr, *Angew. Chem., Int. Ed.*, 2016, **55**, 5749; (e) A. Ghosh, O. F. Mohammed and O. M. Bakr, *Acc. Chem. Res.*, 2018, **51**, 3094; (f) Y. Wang, H. Su, L. Ren, S. Malola, S. Lin, B. K. Teo, H. Häkkinen and N. Zheng, *Angew. Chem., Int. Ed.*, 2016, **55**, 15152; (g) R. P. B. Silalahi, K. K. Chakrahari, J.-H. Liao, S. Kahlal, Y.-C. Liu, M.-H. Chiang, J.-Y. Saillard and C. W. Liu, *Chem.–Asian J.*, 2018, **13**, 500; (h) H. Qian, D. Jiang, G. Li, C. Gayathri, A. Das, R. R. Gil and R. Jin, *J. Am. Chem. Soc.*, 2012, **134**, 16159.

5 (a) F. Olbrich, J. Kopf and E. Weiss, *Angew. Chem., Int. Ed.*, 1993, **32**, 1077; (b) T. C. Higgs, P. J. Bailey, S. Parsons and P. A. Tasker, *Angew. Chem., Int. Ed.*, 2002, **41**, 3038; (c) S. S. Y. Chui, M. F. Y. Ng and C.-M. Che, *Chem.–Eur. J.*, 2005, **11**, 1739; (d) X. Y. Chang, K. H. Low, J. Y. Wang, J. S. Huang and C.-M. Che, *Angew. Chem., Int. Ed.*, 2016, **55**, 10312; (e) G.-C. Kuang, P. M. Guha, W. S. Brotherton, J. T. Simmons, L. A. Stankee, B. T. Nguyen, R. J. Clark and L. Zhu, *J. Am. Chem. Soc.*, 2011, **133**, 13984; (f) H. Lang, A. Jakob and B. Milde, *Organometallics*, 2012, **31**, 7661.

6 A. W. Cook, Z. R. Jones, G. Wu, S. L. Scott and T. W. Hayton, *J. Am. Chem. Soc.*, 2018, **140**, 394.

7 P. Yuan, R. H. Chen, X. M. Zhang, F. J. Chen, J. Z. Yan, C. F. Sun, D. H. Ou, J. Peng, S. C. Lin, Z. C. Tang, B. K. Teo, L. S. Zheng and N. F. Zheng, *Angew. Chem., Int. Ed.*, 2019, **58**, 835.

8 (a) L.-M. Zhang and T. C. W. Mak, *J. Am. Chem. Soc.*, 2016, **138**, 2909; (b) L. L.-M. Zhang and T. C. W. Mak, *Angew. Chem., Int. Ed.*, 2017, **56**, 16228.

9 (a) I. Chakraborty and T. Pradeep, *Chem. Rev.*, 2017, **117**, 8208; (b) B. Nieto-Ortega and T. Bürgi, *Acc. Chem. Res.*, 2018, **51**, 2811; (c) K. Kwak and D. Lee, *Acc. Chem. Res.*, 2019, **52**, 12; (d) R. Jin, C. Zeng, M. Zhou and Y. Chen, *Chem. Rev.*, 2016, **116**, 10346.

10 Y.-P. Xie, J.-B. Wen, C.-W. Pan, G.-X. Duan, L.-Y. Li and X. Lu, *Cryst. Growth Des.*, 2019, DOI: 10.1021/acs.cgd.9b00803.

11 (a) Y.-P. Xie and T. C. W. Mak, *J. Am. Chem. Soc.*, 2011, **133**, 3760; (b) Y.-P. Xie and T. C. W. Mak, *Angew. Chem., Int. Ed.*, 2012, **51**, 8783; (c) Y.-P. Xie, J.-L. Jin, X. Lu and T. C. W. Mak, *Angew. Chem., Int. Ed.*, 2015, **54**, 15176; (d) Y.-P. Xie and T. C. W. Mak, *Chem. Commun.*, 2012, **48**, 1123; (e) G.-X. Duan, Y.-P. Xie, J.-L. Jin, L.-P. Bao, X. Lu and T. C. W. Mak, *Chem.–Eur. J.*, 2018, **24**, 6662; (f) G.-G. Gao, P.-S. Cheng and T. C. W. Mak, *J. Am. Chem. Soc.*, 2009, **131**, 18257; (g) H. Liu, C.-Y. Song, R.-W. Huang, Y. Zhang, H. Xu, M.-J. Li, S.-Q. Zang and G.-G. Gao, *Angew. Chem., Int. Ed.*, 2016, **55**, 3699.

12 I. D. Brown and D. Altermatt, *Acta Crystallogr., Sect. B: Struct. Sci., Cryst. Eng. Mater.*, 1985, **41**, 244.

13 (a) D. Armentano, T. F. Mastropietro, M. Julve, R. Rossi, P. Rossi and G. De Munno, *J. Am. Chem. Soc.*, 2007, **129**, 2740; (b) V. Shivaiah and S. K. Das, *Angew. Chem., Int. Ed.*, 2006, **45**, 245; (c) E. Faggi, R. Gavara, M. Bolte, L. Fajarí,

L. Juliá, L. Rodríguez and I. Alfonso, *Dalton Trans.*, 2015, **44**, 12700.

14 S. Evariste, A. M. Khalil, M. E. Moussa, A. K.-W. Chan, E. Y.-H. Hong, H.-L. Wong, B. L. Guennic, G. Calvez, K. Costuas, V. W.-W. Yam and C. Lescop, *J. Am. Chem. Soc.*, 2018, **140**, 12521.

15 (*a*) T. Sajoto, P. I. Djurovich, A. B. Tamayo, J. Oxgaard, W. A. Goddard and M. E. Thompson, *J. Am. Chem. Soc.*, 2009, **131**, 9813; (*b*) T. Hofbeck, U. Monkowius and H. Yersin, *J. Am. Chem. Soc.*, 2015, **137**, 399; (*c*) M. J. Leitl, V. A. Krylova, P. I. Djurovich, M. E. Thompson and H. Yersin, *J. Am. Chem. Soc.*, 2014, **136**, 16032; (*d*) R. Czerwieniec, M. J. Leitl, H. H. H. Homeier and H. Yersin, *Coord. Chem. Rev.*, 2016, **325**, 2; (*e*) T. J. Feuerstein, B. Goswami, P. Rauthe, R. Köppe, S. Lebedkin, M. M. Kappesbc and P. W. Roesky, *Chem. Sci.*, 2019, **10**, 4742.

16 G. Li, R. S. Nobuyasu, B. Zhang, Y. Geng, B. Yao, Z. Xie, D. Zhu, G. Shan, W. Che, L. Yan, Z. Su, F. B. Dias and M. R. Bryce, *Chem.–Eur. J.*, 2017, **23**, 11761.

17 (*a*) G. Kresse, *J. Non-Cryst. Solids*, 1995, **192–193**, 222; (*b*) G. Kresse and J. Hafner, *Phys. Rev. B: Condens. Matter Mater. Phys.*, 1994, **49**, 14251; (*c*) G. Kresse and J. Furthmuller, *Comput. Mater. Sci.*, 1996, **6**, 15; (*d*) G. Kresse and J. Furthmuller, *Phys. Rev. B: Condens. Matter Mater. Phys.*, 1996, **54**, 11169.

18 (*a*) J. P. Perdew, K. Burke and M. Ernzerhof, *Phys. Rev. Lett.*, 1996, **77**, 3865; (*b*) P. E. Blöchl, *Phys. Rev. B: Condens. Matter Mater. Phys.*, 1994, **50**, 17953.

19 (*a*) H.-Y. Zhuo, H.-F. Su, Z.-Z. Cao, W. Liu, S.-A. Wang, L. Feng, G.-L. Zhuang, S.-C. Lin, M. Kurmoo, C.-H. Tung, D. Sun and L.-S. Zheng, *Chem.–Eur. J.*, 2016, **22**, 17619; (*b*) H.-Y. Zhuo, A.-Y. Hu, L. Feng, Q.-Y. Liu, X.-P. Wang and D. Sun, *J. Cluster Sci.*, 2018, **29**, 1017.

20 (*a*) C. Chan, K. Cheung, W. H. Lam, E. C. Cheng, N. Zhu, S. W. Choi and V. W.-W. Yam, *Chem.–Asian J.*, 2006, **1**, 273; (*b*) W.-Y. Lo, C.-H. Lam, V. W.-W. Yam, N. Zhu, K.-K. Cheung, S. Fathallah, S. Messaoudi, B. L. Guennic, S. Kahlal and J.-F. Halet, *J. Am. Chem. Soc.*, 2004, **126**, 7300; (*c*) G. F. Manbeck, W. W. Brennessel, R. A. Stockland and R. Eisenberg, *J. Am. Chem. Soc.*, 2010, **132**, 12307; (*d*) S. Ibáñez, M. Poyatos and E. Peris, *Angew. Chem., Int. Ed.*, 2018, **57**, 16816.

21 (*a*) S. Chen, W.-H. Fang, L. Zhang and J. Zhang, *Angew. Chem., Int. Ed.*, 2018, **57**, 11252; (*b*) X. Ma, C.-S. Lin, X.-Q. Zhu, S.-M. Hu, T.-L. Sheng and X.-T. Wu, *Angew. Chem., Int. Ed.*, 2017, **56**, 1605; (*c*) R.-W. Huang, Q.-Q. Xu, H.-L. Lu, X.-K. Guo, S.-Q. Zang, G.-G. Gao, M.-S. Tang and T. C. W. Mak, *Nanoscale*, 2015, **7**, 7151; (*d*) Y. Xiao and Q.-M. Wang, *Chem.–Eur. J.*, 2012, **18**, 11184.

22 (*a*) M. Galchenko, A. Black, L. Heymann and C. Klinke, *Adv. Mater.*, 2019, **31**, 1900684; (*b*) F. A. Brede, J. Heine, G. Sextl and K. Müller-Buschbaum, *Chem.–Eur. J.*, 2016, **22**, 2708.

23 (*a*) J. Park, A. C. Hinckley, Z. H. Huang, D. W. Feng, A. A. Yakovenko, M. Lee, S. C. Chen, X. D. Zou and Z. N. Bao, *J. Am. Chem. Soc.*, 2018, **140**, 14533; (*b*) H. Nagatomi, N. Yanai, T. Yamada, K. Shiraishi and N. Kimizuka, *Chem.–Eur. J.*, 2018, **24**, 1806; (*c*) F. Yu, J. Li, Z.-H. Cao, M. Kurmoo and J.-L. Zuo, *Inorg. Chem.*, 2018, **57**, 3443.

24 (*a*) J. A. DeGayner, I.-R. Jeon, L. Sun, M. Dincă and T. D. Harris, *J. Am. Chem. Soc.*, 2017, **139**, 4175; (*b*) I.-R. Jeon, L. Sun, B. Negru, R. P. V. Duyne, M. Dinca and T. D. Harris, *J. Am. Chem. Soc.*, 2016, **138**, 6583; (*c*) L. J. Liu, J. A. DeGayner, L. Sun, D. Z. Zee and T. D. Harris, *Chem. Sci.*, 2019, **10**, 4652.